



Dynamic Compression–Shear Response and Failure Criterion of Rocks with Hydrostatic Confining Pressure: An Experimental Investigation

Hongbo Du¹ · Feng Dai¹ · Mingdong Wei¹ · Ang Li¹ · Zelin Yan¹

Received: 8 April 2020 / Accepted: 31 October 2020 / Published online: 23 November 2020
© Springer-Verlag GmbH Austria, part of Springer Nature 2020

Abstract

Rocks in the deep underground are likely subjected to both hydrostatic confining pressure and dynamic compression–shear load. Thus, accurately characterizing the dynamic properties and failure mechanism of hydrostatically confined rocks under combined compression–shear impacting is crucial for the stability assessment of deep underground rock structures. In this study, on the basis of an improved split Hopkinson pressure bar (SHPB) apparatus, the combined dynamic compression–shear tests are performed on inclined cylindrical sandstone specimens with hydrostatic confining pressures. During the test, the dynamic force balance of rock specimens can be well satisfied using the pulse shaping technique. Our results show that the hydrostatic confining pressure and dynamic loading rate help strengthen the load-carrying capacity of rocks. In contrast, the shear component in the dynamic load limits the dynamic peak stress of rocks. As hydrostatic confining pressure increases, the failure surface based on the Drucker–Prager criterion gradually expands outward. Under dynamic loading, the compressive deformation modulus of rocks decreases with increasing shear component in the dynamic load, contrary to its response to hydrostatic confining pressure. Fragmentation analysis indicates that the hydrostatic confining pressure and the shear component of dynamic loading restrict the fracture behavior of rocks. Besides, as the specimen inclination angle and the hydrostatic confining pressure increase, the failure pattern of rock specimens changes from the tensile-dominated failure with a truncated conical surface to the shear-dominated failure with a single shear plane along its short diagonal.

Keywords Hydrostatic confinement · Dynamic compression–shear load · SHPB · Rate dependence · Drucker–Prager criterion

1 Introduction

Since the gradually exhausted shallow resources are insufficient to meet the rapidly growing demand for energy and spaces, many engineering projects are extended to deep underground (Wagner 2019; Xie et al. 2019). Hundreds of rock engineering in South Africa, Canada, China, and other countries are deepening to underground more than 1000 m. Rocks in such environments are commonly subjected to in-situ hydrostatic confinement and dynamic disturbance simultaneously. The static in-situ stress arises from the gravity stress and tectonic stress, and the dynamic load commonly originates from the drilling, blasting, or earthquakes (Du

et al. 2016; Duan et al. 2019; Hokka et al. 2016; Martin et al. 2013). Moreover, the arbitrary locations of dynamic resources and unpredictable structural surfaces in the rock masses complicate the dynamic loading paths on the highly pressurized rocks, resulting in a combined compression–shear dynamic load. The dynamic responses and failure mechanism of hydrostatically pressurized rocks under combined compression–shear impacting is of considerable significance to the structural integrity and stability in deep underground rock engineering.

Numerous efforts (Frew et al. 2001; Perkins et al. 1970; Xia et al. 2008; Zhang and Zhao 2014) have been made to investigate the effect of pure dynamic load on mechanical properties of rock using the split Hopkinson pressure bar (SHPB) (Hopkinson 1914; Kolsky 1949), and they reported that the dynamic mechanical responses of rocks were highly loading rate dependent. However, in the underground, rocks suffer from the static in-situ stress before the dynamic disturbance, leading to a coupled static and dynamic stress

✉ Mingdong Wei
weimingdong@163.com

¹ State Key Laboratory of Hydraulics and Mountain River Engineering, College of Water Resources and Hydropower, Sichuan University, Chengdu 610065, Sichuan, China

state (Li et al. 2008, 2017). Few investigations have paid attention to the coupled static–dynamic loading effect on the rock properties. Li et al. (2008) investigated the mechanical responses of rock under one-dimensional coupled load, and they found that the dynamic mechanical properties and failure modes of rock under coupled static–dynamic loading conditions were quite different from those subjected to static or dynamic load solely. In recent years, some researchers (Bailly et al. 2011; Du et al. 2018; Frew et al. 2010; Gong et al. 2019; Hokka et al. 2016) studied the effect of three-dimensional coupled static–dynamic load on rock properties, and their results indicated that the radial confining pressure significantly enhanced the load-carrying capacity of rocks. In particular, the hydrostatic confining pressure is likely encountered at the depth below 1000 m (Wagner 2019; Xie et al. 2019). Thus, accurately characterizing the dynamic responses and failure mechanism of hydrostatically pressurized rocks is of great concern for deep underground engineering excavations.

In practical underground engineering, rocks are generally loaded with a complex loading path rather than a single compression or shear load, and the combined compression–shear load is commonly encountered due to the arbitrary location of dynamic loading sources and structural surfaces in rock masses. Pillars in underground engineering have more or less an inclination angle with the vertical direction, leading to a combined compression–shear load. Foroughi and Vutukuri (1997) realized that the shear component complicated the stability evaluation of pillars. Suorineni et al. (2011, 2014) further reported that the compressive load-carrying capacity of rock decreased with the increasing inclination angle. The shear component in the load also has a significant influence on the fracture behavior of rocks (Duan et al. 2019; Li et al. 2019; Zhao et al. 2018). In dynamic rock experiments, the combined compression–shear loading is commonly achieved via two methods, i.e., modifying the SHPB testing apparatus or employing specially designed specimens. For the first method, the specific SHPB apparatus has been modified in previous attempts, including using an incident bar with a wedge-shaped end and two transmitted bars (Zhao et al. 2012) or adding cushions with designed beveled surfaces at the close-to-specimen ends of the incident and transmitted bars (Hou et al. 2011, 2019; Xu et al. 2015; Zhao et al. 2011). For the second method, the inclined specimens were used to achieve dynamic compression–shear loading (Du et al. 2020a; Nie et al. 2007; Sun et al. 2009; Xu et al. 2020; Xu and Dai 2018). In these studies, the loading rate sensitivity and loading path dependency of dynamic response have been systematically investigated, in terms of the compressive and shear dynamic peak stresses, deformation modulus, and even the failure processes of specimens. In our previous work (Du et al. 2020a), we conducted experimental and numerical SHPB tests only on the inclined specimens with

an inclination angle of 5° . It mainly focused on the influence of hydrostatic confinement on the mechanical response and failure mechanism of this particular sample geometry (5°). The dynamic load-carrying ability and the deformation property of 5° specimens were investigated experimentally, and corresponding numerical simulations were performed to reveal the progressive failure of the specimen. However, the influences of different shear/compression ratios on the tests have not been revealed. Moreover, the failure criterion of hydrostatically confined rocks under various combined compression–shear impacting conditions has not been studied yet.

In this paper, hydrostatic confining pressures are integrated with various combined compression–shear impacting conditions by introducing different inclined cylindrical rock specimens into the SHPB apparatus modified with axial and radial confining systems. To further investigate the dynamic mechanical response and failure mechanism of rock under combined compression–shear impacting, a series of tests are carried out on sandstone specimens with different inclination angles under hydrostatic confinements of 7, 14, 21, and 28 MPa. The comprehensive effects of the shear/compression ratio (related to the specimen inclination angle), hydrostatic confining pressure, and dynamic loading rate on the dynamic peak stress, deformation modulus, and fragmentation and failure patterns of rock are systematically analyzed. Moreover, under different hydrostatic confining pressures, the failure criterion of rocks subjected to compression–shear impacting is explored.

2 Experimental Procedures

2.1 Testing Apparatus

The compression–shear impacting experiments on hydrostatically pressurized rock specimens are conducted on an improved SHPB apparatus, as shown in Fig. 1. This apparatus comprises three bars, an axial pre-compression stress inducer, a radial confining pressure inducer, and a data monitoring unit. The three elastic bars (i.e., striker, incident bar, and transmitted bar) are 50 mm in diameter and 0.3 m, 3 m, and 2 m in length, respectively, which are made of ultrahigh strength steel with density and elastic modulus of 7800 kg/m^3 and 221 GPa, respectively. By referring to the suggestions for SHPB compression tests on brittle material by Frew et al. (2002) and Dai et al. (2010), a thin copper disc is placed at the free end of the incident bar acting as a pulse shaper to generate a ramped shape incident pulse, which facilitates the dynamic stress balance of specimens during the dynamic loading process.

The axial confining system consists of three main parts: (1) a cylindrical chamber located at the far end of the

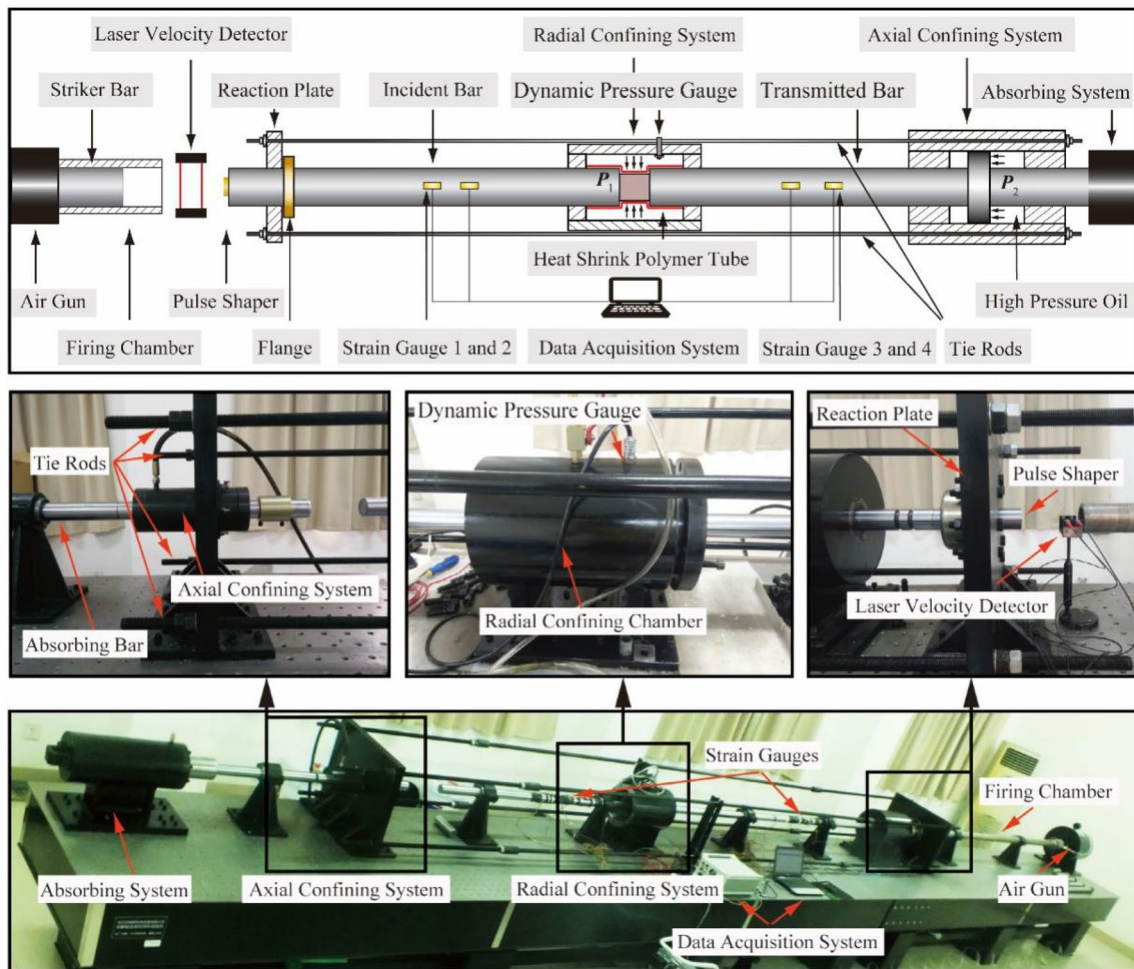


Fig. 1 Split Hopkinson pressure bar (SHPB) apparatus modified with axial and radial confining systems (Du et al. 2020a)

transmitted bar to supply the axial compressive load, (2) a rigid reaction plate with a flange, placed at the impacting end of the incident bar to restrict its leftward movement, and (3) four tie rods connecting the axial confining chamber and the reaction plate to minimize the potential bending moment induced by the axial pre-load. As for the lateral confining pressure system, it is composed of a larger hydraulic vessel with two seal end caps for installing the specimen and two valves mounted on the bottom and top positions of the vessel, respectively. The hydraulic oil gets into the cell through the inlet valve at the bottom, and the gas escapes from the outlet valve at the top. It is worth noting that the radial confining chamber is fabricated to own a large cubage to minimize the variation of confining pressure during dynamic loading, and the actual confinement at any instant is detected by a high-frequency pressure detector mounted on the top position of the vessel (Fig. 1).

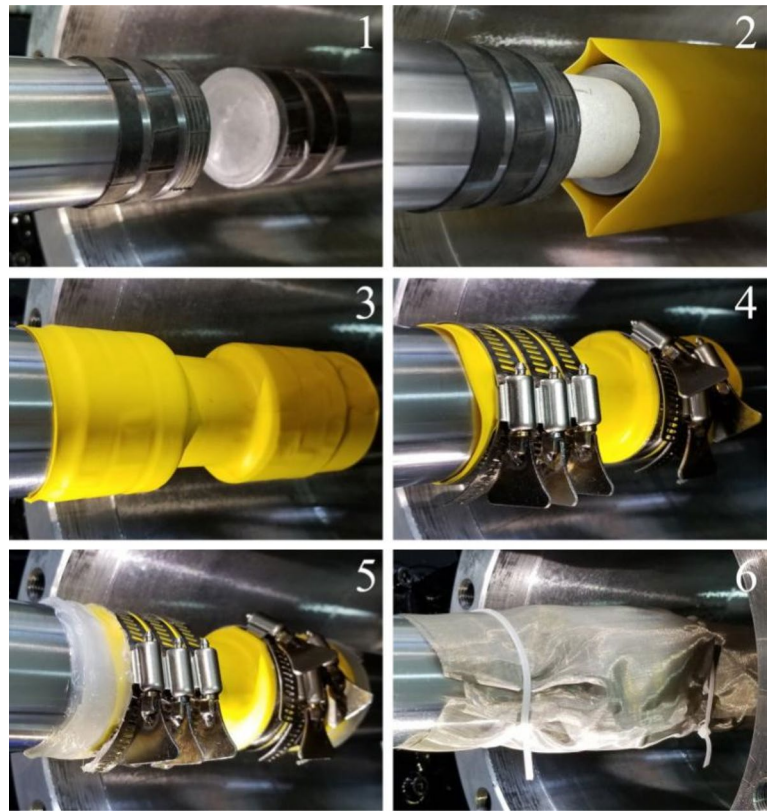
Before applying the axial and radial confining pressures, the rock specimen should be well sealed to prevent hydraulic oils from permeating the pores of the specimen and the

bar–specimen interfaces. As shown in Fig. 2, the specimen sealing process contains the following six steps: (1) the ends of the incident and transmitted bars near the specimen are both circled with three rubber bands; (2) the specimen is sandwiched between the incident and transmitted bars; (3) a heat shrink polymer tube is heated to cling on the surfaces of rubber bands and specimen; (4) the hose clamps at the superficial positions of rubber bands are frapped to ensure good contact between the bar and the heat shrink tubes; (5) the hot-melt adhesive is smeared evenly on the two ends of heat shrink tube to prevent the pressurized hydraulic oil from permeating the interface between heat shrink tube and bars; and (6) the strainer coating is employed to finish the sealing process for collecting the fragments of rock specimens once the sealing system is punctured.

2.2 Data Processing

Once the specimen is well sealed, the axial and radial confining pressures are applied to the specified levels via a

Fig. 2 Sealing process of a hydrostatically confined specimen in the dynamic compression–shear test



hydraulic pressure supply system with an operating pressure of 40 MPa. The compressed air is then released to drive the striker to impact on the pulse shaper prior to the incident bar, generating a shaped stress pulse. Two groups of strain gauges mounted in the middle positions of the incident bar and transmitted bars are utilized to monitor the strain signals, including the incident strain (ϵ_i), reflected strain (ϵ_r), and transmitted strain (ϵ_t). The force applied on the incident end of the specimen (P_1) can be represented by the superposition of incident and reflected pulses, while the force acting on the transmitted end of the specimen (P_2) can be derived from the transmitted pulse:

$$P_1 = A_b E_b (\epsilon_i + \epsilon_r), P_2 = A_b E_b \epsilon_t, \quad (1)$$

where A_b and E_b are the cross-sectional area and elastic modulus of the bar, respectively. According to Li et al. (2008), the stress wave propagation in the axial pre-stressed bars is unaffected by the pre-load. The forces acting on the incident and transmitted ends of specimens can be deduced from the incident, transmitted, and reflected strain signals using Eq. (1). However, with further consultation with Chen et al. (2018), an additional stress wave (detachment wave) with the magnitude of σ_{pre} is generated after the incident pulse. If the detachment wave arrives at the strain gauge after the end of the reflected pulse, the equation mentioned above could be directly employed in our hydrostatic confining SHPB tests.

Thus, the following prerequisite should be satisfied before the dynamic force equilibrium check:

$$\sigma_{\text{pre}} < \frac{\rho v_0 L_0 C}{2(L_i - L_c)}, \quad (2)$$

where ρ stands for the striker density, v_0 and C are the moving velocity and longitudinal wave velocity of striker, L_0 and L_i represent the lengths of striker and incident bar, and L_c denotes the distance between the strain gauge on the incident bar and the reaction plate. In our experiments, the striker moves faster than 9 m/s, and the corresponding σ_{pre} is 36.5 MPa. This threshold is satisfied in our tests, and thus dynamic force equilibrium can also be depicted by the conventional equation (Eq. 1). If the force equilibrium ($P_1 = P_2$) is satisfied, the dynamic deviatoric compressive stress (σ_{dyn}) and strain (ϵ_{dyn}) can be expressed as follows:

$$\begin{cases} \epsilon_{\text{dyn}}(t) = -\frac{2C}{L} \int_0^t \epsilon_r dt \\ \sigma_{\text{dyn}}(t) = \frac{A_b}{A_0} E_b (\epsilon_t - \epsilon_{\text{pre}}) \end{cases}, \quad (3)$$

where A_0 is the contact area between the specimen and bars, and ϵ_{pre} is the strain caused by the pre-stress. Since the hydrostatic confining pressure cannot cause shear stress or

shear strain, the average shear stress (τ) on the bars–specimen interface can be calculated from the dynamic deviatoric compressive stress only:

$$\tau(t) = \sigma_{\text{dyn}}(t) \tan \theta. \tag{4}$$

Considering the triaxial stress state of the specimen in our tests, the Drucker–Prager criterion (Drucker and Prager, 1952) is utilized hereafter to describe the failure mechanism of rocks with hydrostatic confining pressure in combined compression–shear impacting tests. This criterion has been widely employed to investigate the pressure-related failure behavior of rocks in recent years (Rahimi and Nygaard 2015; Xu et al. 2015; Xu and Dai 2018). The criterion can be expressed as:

$$\sqrt{J_2} = \alpha I_1 + k, \tag{5}$$

where I_1 and J_2 are the first invariant of stress tensor and the second invariant of the deviatoric stress tensor, respectively; α and k are material constants related to the confining pressure and stress state. In the present study, $I_1 = \sigma_{\text{dyn}} + 3\sigma_{\text{pre}}$, $J_2 = \frac{1}{3}\sigma_{\text{dyn}}^2 + \tau^2$, and thus the D–P criterion in the $\sigma - \tau$ plane can be interpreted as

$$\sqrt{\frac{1}{3}\sigma_{\text{dyn}}^2 + \tau^2} = \alpha(\sigma_{\text{dyn}} + 3\sigma_{\text{pre}}) + k. \tag{6}$$

Due to the existence of the shear component in the dynamic load, it is inappropriate to determine the loading rate from the compressive load solely. Considering the dynamic equivalent stress ($\sigma_e = \sqrt{\sigma_{\text{dyn}}^2 + 3\tau^2}$) is deduced from the dynamic deviatoric compressive stress and the

dynamic shear stress, it has been introduced as a characteristic variable in the compression–shear impacting tests (Nie et al. 2007). As shown in Fig. 3, the slope of the linear portion of dynamic equivalent stress evolution before peak stress is defined as the dynamic equivalent stress rate ($\dot{\sigma}_e$), which is employed here to characterize the loading rate in dynamic compression–shear tests.

2.3 Specimen Preparation

The sandstone in this study is taken from the Neijiang city, Sichuan province, China. To determine its nominal mineral composition and texture, a thin section is sliced and polished for the petrographic study under the plane-polarized light and cross-polarized light (Fig. 4). This sandstone is composed of 43% feldspar, 35% quartz, 20% rock fragments, and 2% clay minerals in volumetric fraction. The mineral grain sizes are in the range of 0.2–0.3 mm. According to Green-smith (1983), this rock material is classified as fine-grained feldspathic sandstone with pore cementation.

By referring to the ISRM-suggested method for dynamic compression tests (Zhou et al. 2012), the specimens are designed to have the length (L) of 38 mm and the diameter (D) of 38 mm (i.e., a slenderness ratio of 1:1). The core axes of the specimens are inclined to the loading direction, forming inclination angles (θ). Two ends of the specimen are polished with specific cutters (Xu and Dai 2018) to achieve two parallel end surfaces. The tolerances of planeness and parallelism are restricted to be smaller than 0.05 mm and 0.15°, respectively. In total more than 70 specimens are prepared for this study (Fig. 4). The average longitudinal wave velocity and density of the specimen are 1850 m/s and 2320 kg/m³,

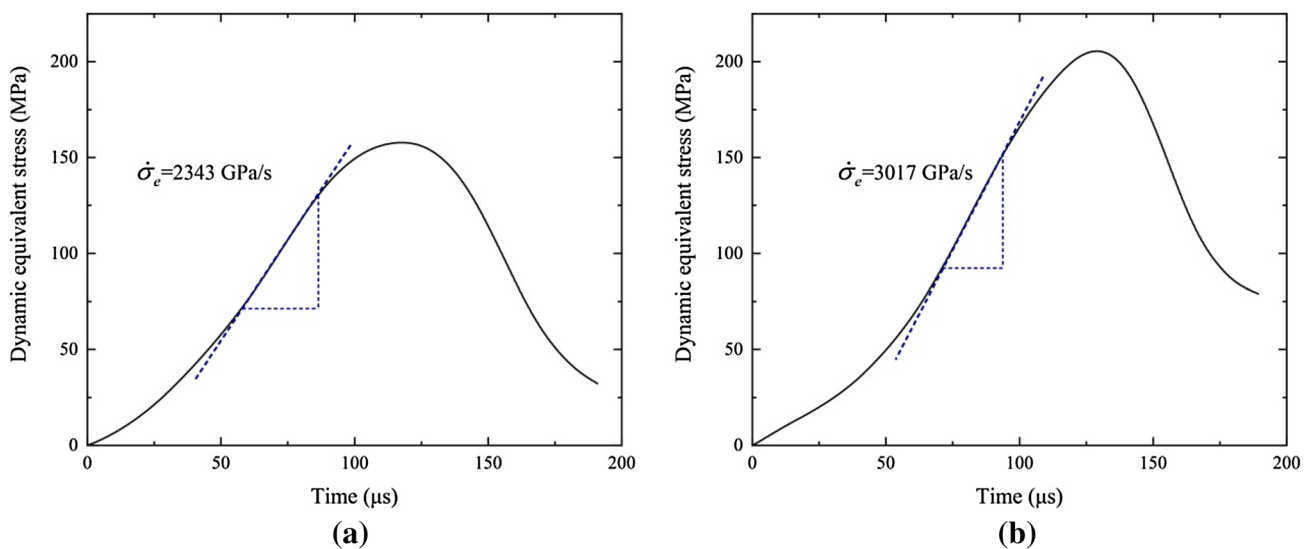


Fig. 3 Equivalent stress evolution of **a** a 3° specimen with hydrostatic confinement of 7 MPa at the dynamic equivalent stress rate of 2343 GPa/s and **b** a 7° specimen with hydrostatic confinement of 21 MPa at the dynamic equivalent stress rate of 3017 GPa/s

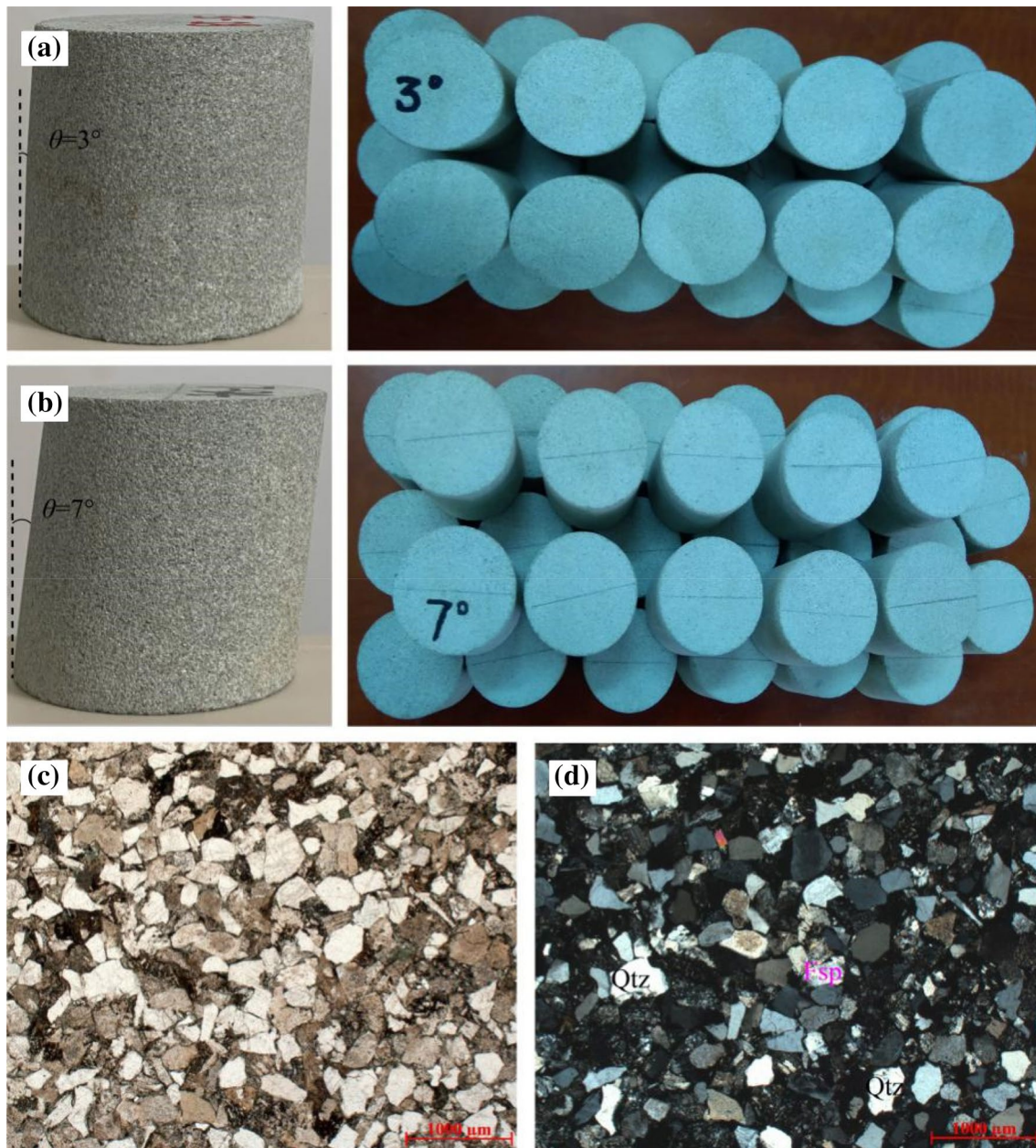


Fig. 4 Prepared sandstone specimens with inclination angles of **a** 3° and **b** 7° ; and the polarized light petrographic micro-images of Neijiang sandstone: **c** plane-polarized light, and **d** cross-polarized light

respectively. Some basic mechanical information of the sandstone is obtained from static tests conducted on the MTS-815 rock testing system at Sichuan University. The compressive and tensile strengths of the sandstone are 70 MPa and 5.4 MPa, respectively. The elastic modulus and Poisson's ratio are 8 GPa and 0.23, respectively.

3 Results and Discussion

In this section, the comprehensive effects of shear/compression ratio (related to the specimen inclination angle), hydrostatic confinement, and dynamic loading rate on the

mechanical response and failure mechanism of rocks are revealed and discussed. For further comparison and discussion, the dynamic peak stress and the dynamic compressive modulus of 0° and 5° specimens from previous studies (Du et al. 2020a, b) are cited here to better and more systematically elucidate the influences of shear/compression ratios on dynamic mechanical properties of hydrostatically pressurized rocks. With the citation to those data, the failure criterion of hydrostatically pressurized rocks under compression–shear impacting can also be assessed more deeply and accurately. Furthermore, the fragmentation and inner failure modes of inclined cylindrical rock specimens under different hydrostatic confinements are presented, which have not been reported in previous studies.

3.1 Dynamic Stress Balance

In this study, a thin copper disc with a 15 mm diameter and 3 mm thickness is employed to act as the pulse shaper. The shaping technique reduces the rising slope and eliminates the high-frequency oscillation of stress waves, forming a half-sine incident pulse to facilitate the stress balance of the specimen during the dynamic loading. Figure 5 shows the dynamic stress balance check for two typical tests on the hydrostatically pressurized rock specimens with inclination angles 3° and 7°. The three letters (I, R, and T) in the two figures denote the incident, reflected, and transmitted waves, respectively, and the superposition of incident and reflected waves is represented by I+R. As shown in the figures, the incident waves are almost in half-sine shape, indicating that

the copper disc pulse shaper works well. The reflected waves initiate from zero, while the others start from the pre-load stresses rather than zero. Before the incident wave arrives at the incident end of the specimen, both the incident and transmitted stresses of the specimen are equal to the pre-load stress, indicating that the pre-load systems are reliable for applying triaxial confining pressure. As the incident wave loads on the specimen, part of it reflects back to the incident bar and produces the tensile reflected wave; the remainder propagates through the specimen to the far end of the transmitted bar, forming the transmitted compressive wave. As shown in Fig. 5, the stress on the incident specimen end (I+R) agrees well with that on the transmitted end (T). The dynamic stress equilibrium of hydrostatically confined rock specimens under different combined compression–shear loads is finely satisfied, indicating that the inertial effect is minimized and the quasi-static data processing method is valid.

3.2 Dynamic Axial Stress–Strain Curves and Deformation Properties

The relationship between dynamic axial compressive stresses and strains of the oblique specimens under dynamic impacting is obtained on the basis of Eq. (3). Figures 6 and 7 illustrate the dynamic axial compressive stress versus strain curves of the specimens with inclination angles 3° and 7° at hydrostatic confining pressures 7, 14, 21, and 28 MPa. The stress–strain curves can be divided into three portions: linear increase stage, yielding stage, and post-failure stage. In the linear stage, the curve rises with a constant slope,

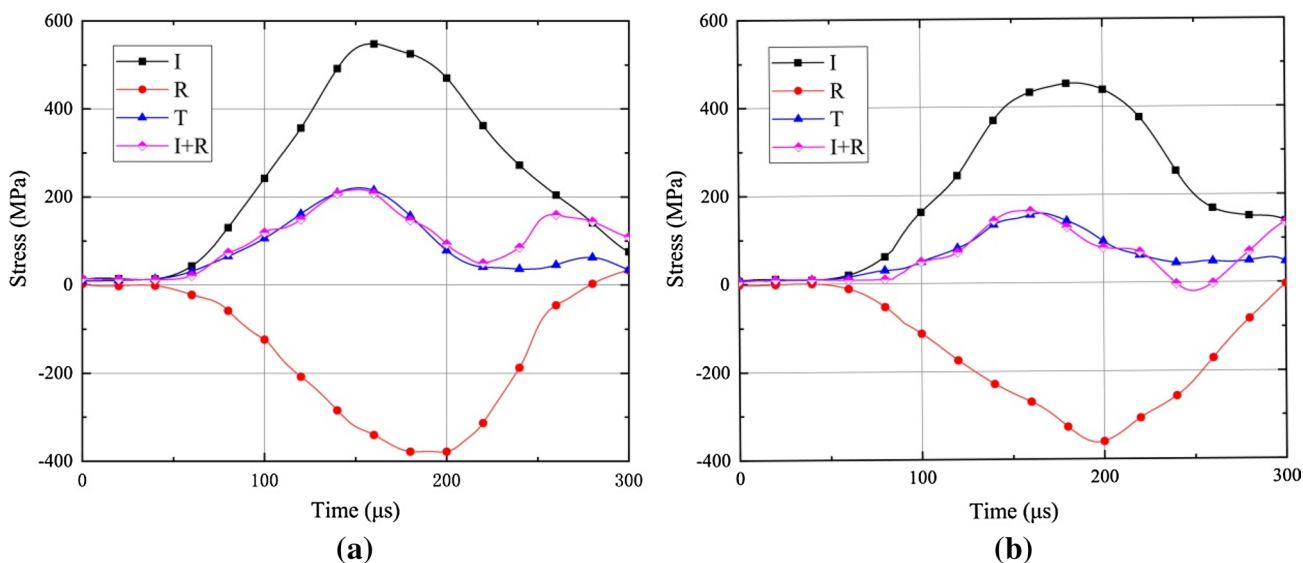


Fig. 5 Dynamic force equilibrium check for typical tests: **a** 3° rock specimen with the hydrostatic confinement of 7 MPa and the dynamic equivalent stress rate of 2811 GPa/s, and the striker velocity is

18.1 m/s; **b** 7° rock specimen with the hydrostatic confinement of 7 MPa and the dynamic equivalent stress rate of 2582 GPa/s, and the striker velocity is 17.7 m/s

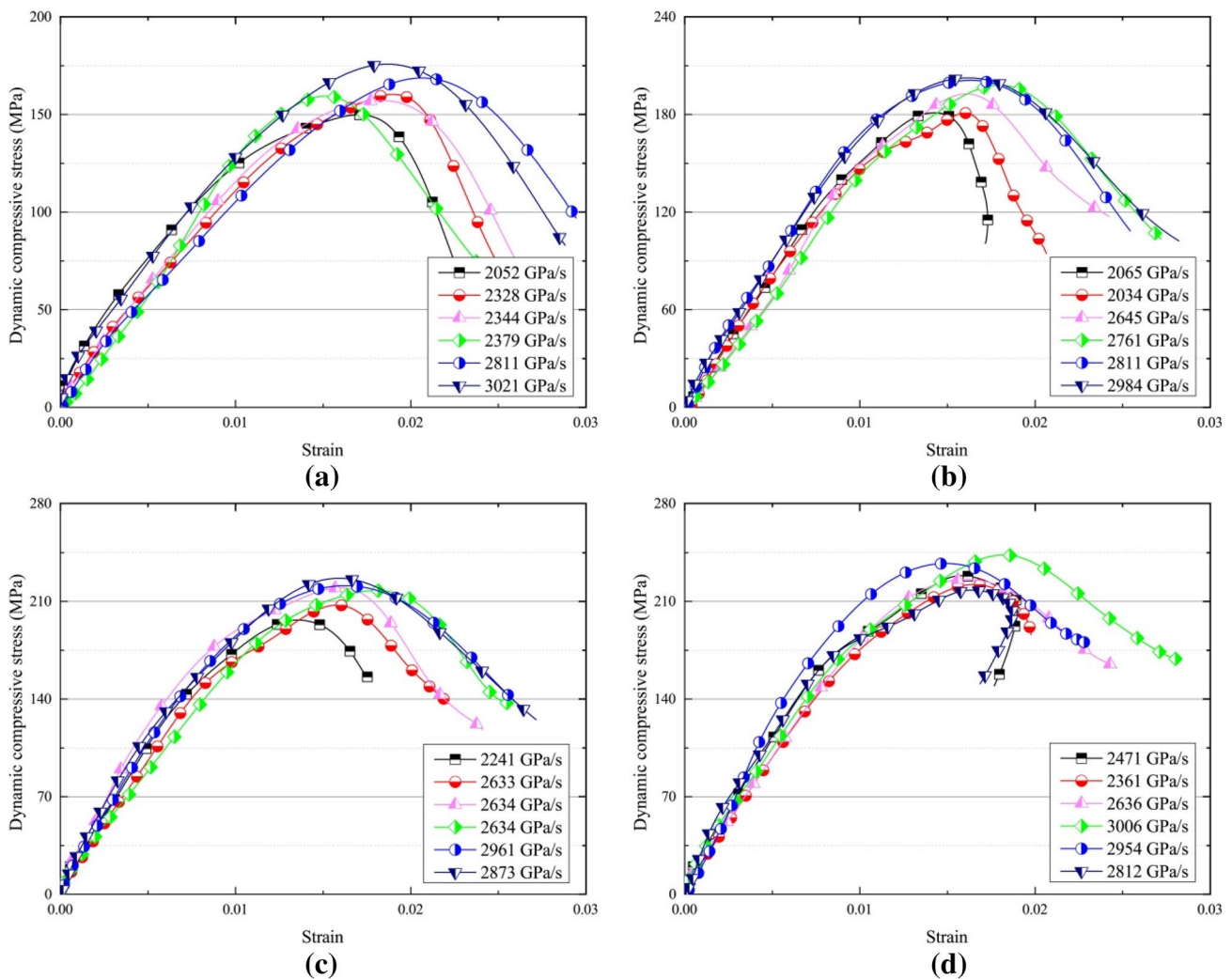


Fig. 6 Dynamic axial compressive stress–strain curves of the 3° specimens under hydrostatic confinements of **a** 7 MPa, **b** 14 MPa, **c** 21 MPa, and **d** 28 MPa

and the dynamic compressive deformation modulus can be determined. Under different dynamic equivalent stress rates, these curves seem to have the same slope, suggesting that the dynamic loading rate has no significant influence on the axial compressive deformation modulus. In the yielding stage, the stress–strain curve becomes nonlinear and its slope becomes smaller and smaller. Subsequently, during the post-failure stage, the load-carrying capacity of the specimen decreases gradually instead of dropping rapidly after the peak, indicating that the ductility of the rock is improved and the brittleness is weakened due to the compaction effect of confining pressure.

The slopes of these curves at their linear increase stages can be employed to characterize the axial deformability of the oblique sandstone specimens with different hydrostatic confinements in the combined compression–shear impacting tests, and the corresponding values under various loading

conditions are tabulated in Tables 1 and 2. For better visualization, the variation trends of the dynamic compressive modulus are fitted using linear curves. Figure 8a exhibits the variation of the dynamic compressive modulus versus the shear component of dynamic peak stress under confining pressures of 7, 14, 21, and 28 MPa. It can be seen that the compressive modulus of hydrostatically pressurized rocks under combined compression–shear impacting decreases with the increase of the shear component of dynamic peak stress. The slope of the fitted curves decreases from -0.24 to -0.48 as the hydrostatic confinement increases from 7 to 28 MPa, indicating that the confining pressure strengthens the weakening effect of the shear component on the compressive deformation modulus. Figure 8b shows a linear change trend of the compressive deformation modulus of the oblique rock specimens with different hydrostatic confining pressures. For a higher confining pressure, the modulus

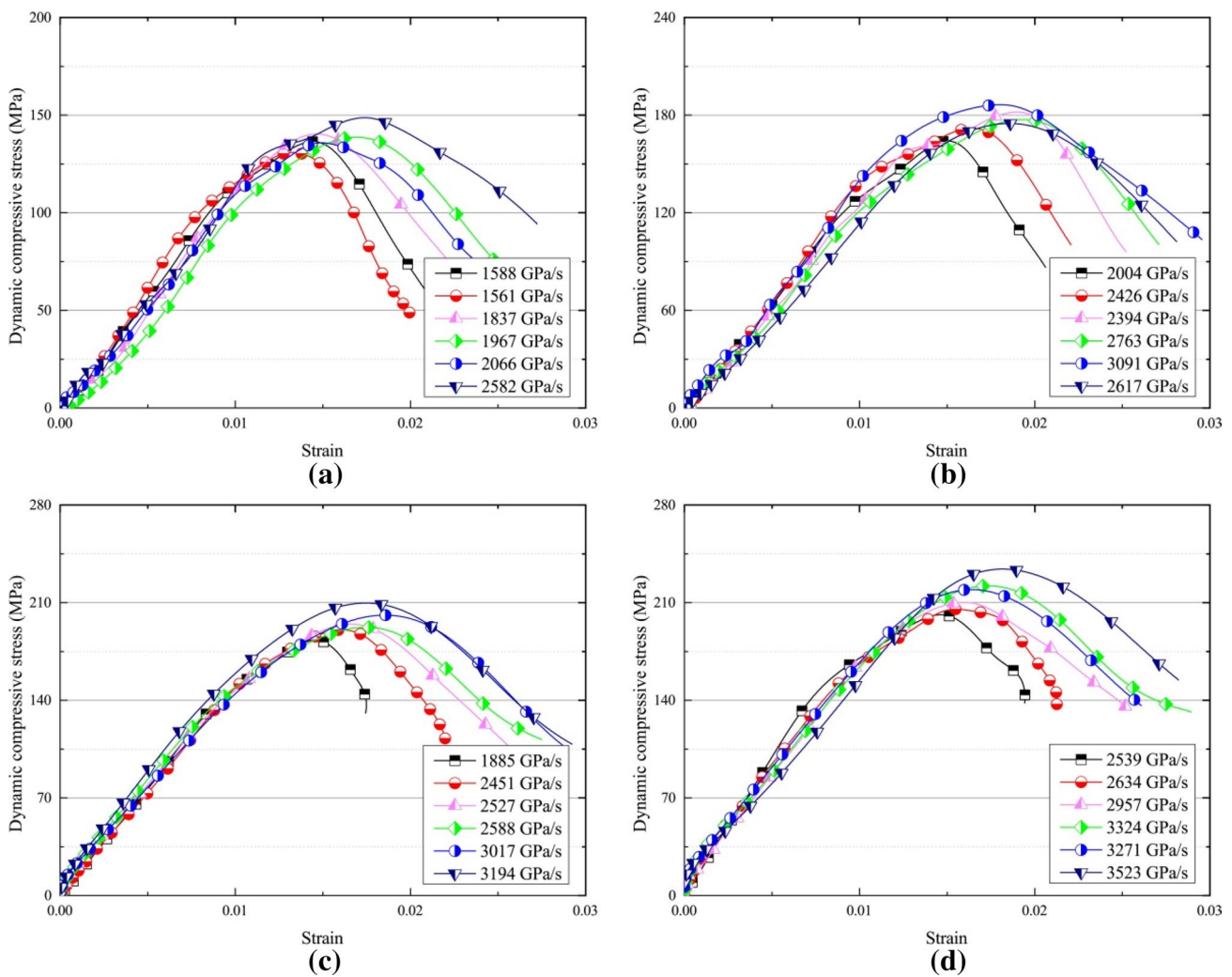


Fig. 7 Dynamic axial compressive stress–strain curves of the 7° specimens under hydrostatic confinements of **a** 7 MPa, **b** 14 MPa, **c** 21 MPa, and **d** 28 MPa

is much larger due to the compaction effect of confinement. As the inclination angle increases from 0° to 7°, the average modulus increments induced by the confinement increasing from 7 to 28 MPa are 13.65, 11.34, 9.659, and 6.72 GPa in order, and the rising slope of curves decreases from 0.65 to 0.32 as well. This result suggests that the enhancement effect of confining pressure on the dynamic compressive modulus of rock is weakened by the increasing shear component in dynamic load.

3.3 Dynamic Peak Stresses and Failure Criterion

In this study, the shear component of dynamic peak stress can be derived from the corresponding axial component using Eq. (4). Figures 9 and 10 depict the axial and shear components of dynamic peak stress varying with the dynamic equivalent stress rate, respectively, and Fig. 11

demonstrates the variation of the maximum principal peak stress under different loading conditions. The axial component of dynamic peak stress and the maximum principal peak stress of sandstone highly depend on the loading rate, compatible with previous studies (Dai et al. 2010; Zhang and Zhao 2014). The increase in the shear component of dynamic loading has a minor effect on the loading rate sensitivity. It can also be seen that the axial component of dynamic peak stress and the maximum principal peak stress of rocks obviously decrease as the inclination angle increases. However, the shear component of dynamic peak stress has the opposite response to the inclination angle; the rock specimen with a larger inclination angle has a larger shear component of dynamic peak stress. Under different hydrostatic confining pressures, the dependence of maximum principal peak stress on the inclination angle has no visible differences. While the hydrostatic confining pressure significantly influences the

Table 1 Axial and shear components of dynamic peak stress and the compressive modulus of 3° sandstone specimens with hydrostatic confinements of 7, 14, 21, and 28 MPa

Hydrostatic confinement (MPa)	Dynamic equivalent stress rate (GPa/s)	Dynamic compressive modulus (GPa)	Axial component of dynamic peak stress (MPa)	Shear component of dynamic peak stress (MPa)
7	2052	11.4	149.8	7.8
	2328	11.3	160.2	8.4
	2343	11.9	157.1	8.2
	2378	11.6	159.4	8.4
	2600	11.6	167	8.8
	2810	10.6	168.7	8.8
	3020	13.1	175.8	9.2
14	2065	15.1	181	9.5
	2034	14.5	180.9	9.5
	2385	14.7	185.2	9.7
	2645	14.9	192.6	10.1
	2760	14	198	10.4
	2810	16.7	201	10.5
	2983	16	202.4	10.6
21	1923	17.8	195.1	10.2
	2240	19.4	196.6	10.3
	2453	19.9	205.3	10.8
	2632	18.4	207.3	10.9
	2634	20.9	219.7	11.5
	2634	16.9	217.8	11.4
	2873	20.3	226.6	11.9
28	2961	20.4	221.2	11.6
	2189	22.3	218	11.4
	2360	21.6	222.1	11.6
	2471	23.6	228.5	12
	2636	22.1	225.9	11.83
	2811	23.9	239	12.5
	2953	24.3	237.2	12.4
	3005	21.3	243.2	12.7

dependence of axial and shear components of dynamic peak stress on the inclination angle. As the confinement increases from 7 to 28 MPa, the decrement of the axial component and the increment of the shear component of dynamic peak stress increase significantly.

To quantitatively characterize the dynamic failure surfaces, the D–P criterion (Eq. 5) and its variant (Eq. 6) are employed herein to illustrate the relationship between the axial and shear components of dynamic peak stress of rocks under different hydrostatic confining pressures. In Fig. 12, the axial and shear components of dynamic peak stress corresponding to the confining pressure of 7, 14, 21, and 28 MPa are plotted in the $I_1 - \sqrt{J_2}$ plane. The D–P criterion (Eq. 5) in this plane features a linear relationship; the material parameters α and k can be determined by the slope and the intercept of the linearly fitted curves. However, the fitted parameters derived from only the $I_1 - \sqrt{J_2}$

plane may be inapplicable in the $\sigma - \tau$ plane (Xu et al. 2015). Thus, the results at different hydrostatic confinements are also sketched in the $\sigma - \tau$ plane, as shown in Fig. 13. According to Eq. (4), four dashed lines are drawn to trace the distribution of data points corresponding to the inclination angles 0°, 3°, 5°, and 7°, respectively, and their slopes represent the ratios between the shear and axial components of dynamic loading. By taking the two planes into consideration, the failure surfaces are fitted using the optimal fitting approach. As shown in Figs. 12 and 13, the fitted failure surfaces match well with the data points in the two planes. As the hydrostatic confining pressure increases from 7 to 28 MPa, the fitted material parameters α and k are 0.5302 and -2.58382 MPa, 0.5265 and -11.62681 MPa, 0.5225 and -20.44187 MPa, 0.519 and -29.23865 MPa in order. It can be found that both α and k show a linearly negative correlation with the

Table 2 Axial and shear components of dynamic peak stress and the compressive modulus of 7° sandstone specimens with hydrostatic confinements of 7, 14, 21, and 28 MPa

Hydrostatic confinement (MPa)	Dynamic equivalent stress rate (GPa/s)	Dynamic compressive modulus (GPa)	Axial component of dynamic peak stress (MPa)	Shear component of dynamic peak stress (MPa)
7	1588	10.8	136.4	16.7
	1561	11.1	130.9	16.1
	1837	10.9	140.3	17.2
	1966	9.7	138.7	17
	2065	10.3	135.8	16.7
	2582	11.4	148.7	18.3
14	3201	11.2	155.3	19.1
	2003	11.8	164.1	20.1
	2393	12.6	181.9	22.3
	2425	13	171.9	21.1
	2617	11.4	174.9	21.5
	2763	11.8	177.2	21.8
21	3090	13.8	186.4	22.9
	1884	14.9	183.1	22.5
	2226	14.7	185	22.7
	2451	14.9	190.4	23.4
	2526	14.6	194.5	23.9
	2588	14.9	192.3	23.6
28	3017	14.3	201	24.7
	3194	16.3	209.7	25.7
	1989	18.2	190	23.3
	2539	19	201.3	24.7
	2633	17.4	205.2	25.2
	2957	17	210.2	25.8
	3271	17.1	219.4	26.9
	3324	16.7	222	27.3
	3523	16	234	28.7

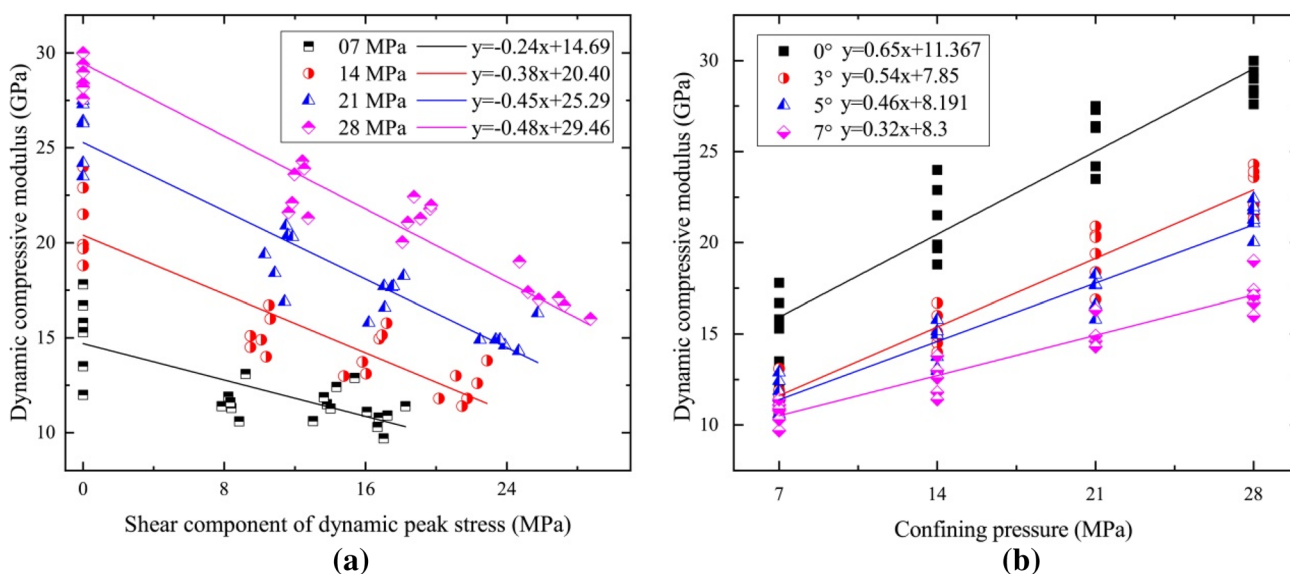


Fig. 8 Dynamic compressive modulus of the rock specimens with different inclination angles under hydrostatic confining pressure

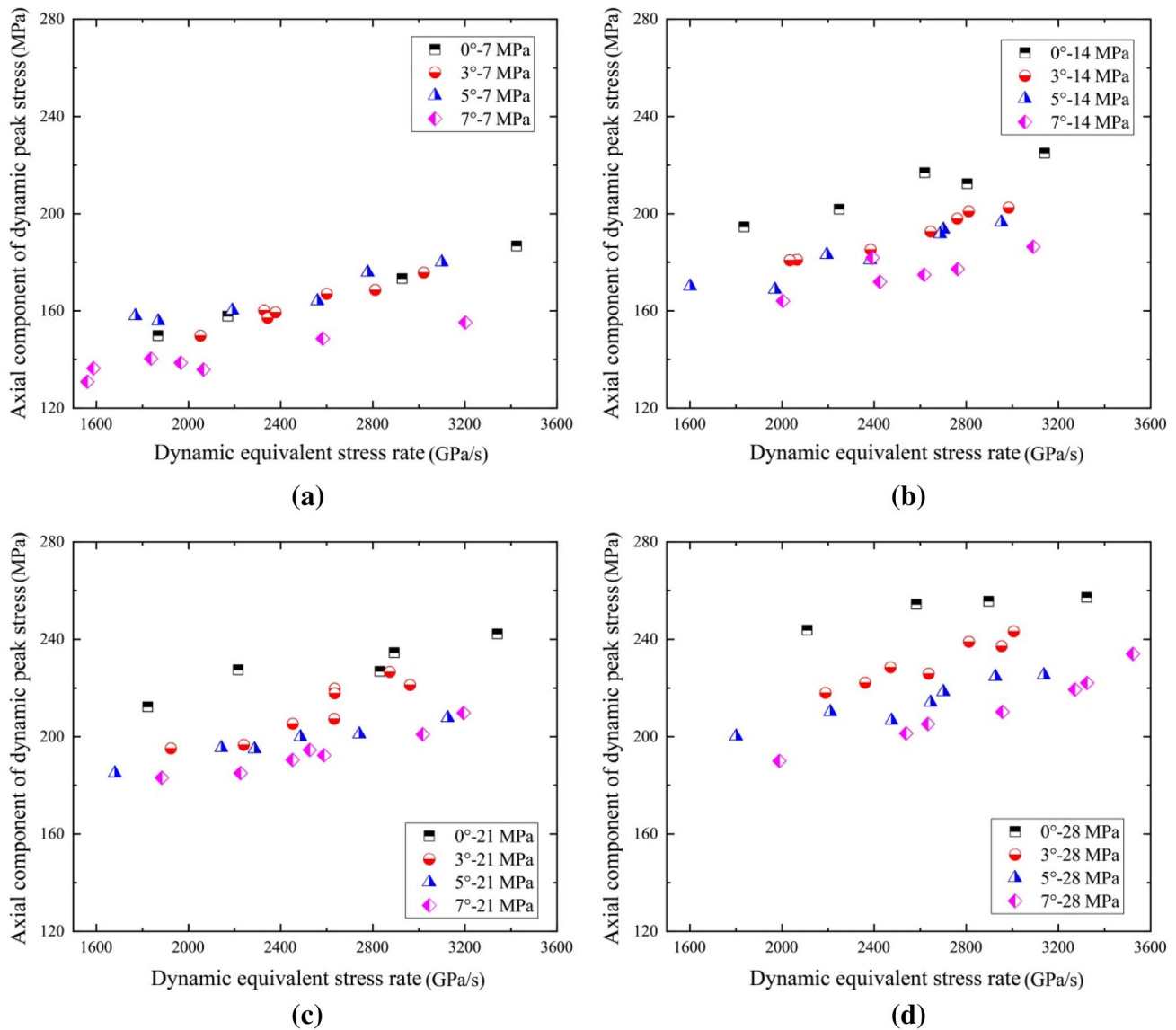


Fig. 9 Axial component of dynamic peak stress of the rock specimens with different inclination angles under various hydrostatic confining pressures

hydrostatic confining pressure. In the $\sigma - \tau$ plane, the failure surface gradually expands outward with the increase of hydrostatic confinement. Figure 13 demonstrates the effects of hydrostatic confining pressure and specimen inclination angle on the dynamic peak stress. A sector is featured by plotting the axial and shear components of dynamic peak stress of hydrostatically pressurized rocks into the $\sigma - \tau$ plane, in which the longitude indicates the shear/compression ratio of the dynamic load, and the latitude represents the failure surface under the same hydrostatic confining pressure.

3.4 Fragmentation and Final Failure Patterns

Because the fragmentation and failure patterns of cylindrical rock specimens have some implications for the potential failure of underground rock structures (Shen et al. 2017), manual sieving and a post-mortem examination are performed on the broken rock specimens. The grading curves of fragments and the failure patterns presented in this section clearly demonstrate the effects of hydrostatic confining pressure and inclination angle on the fracture behavior of rock specimens. To quantitatively characterize the fragmentation of rock specimens under different confinements after

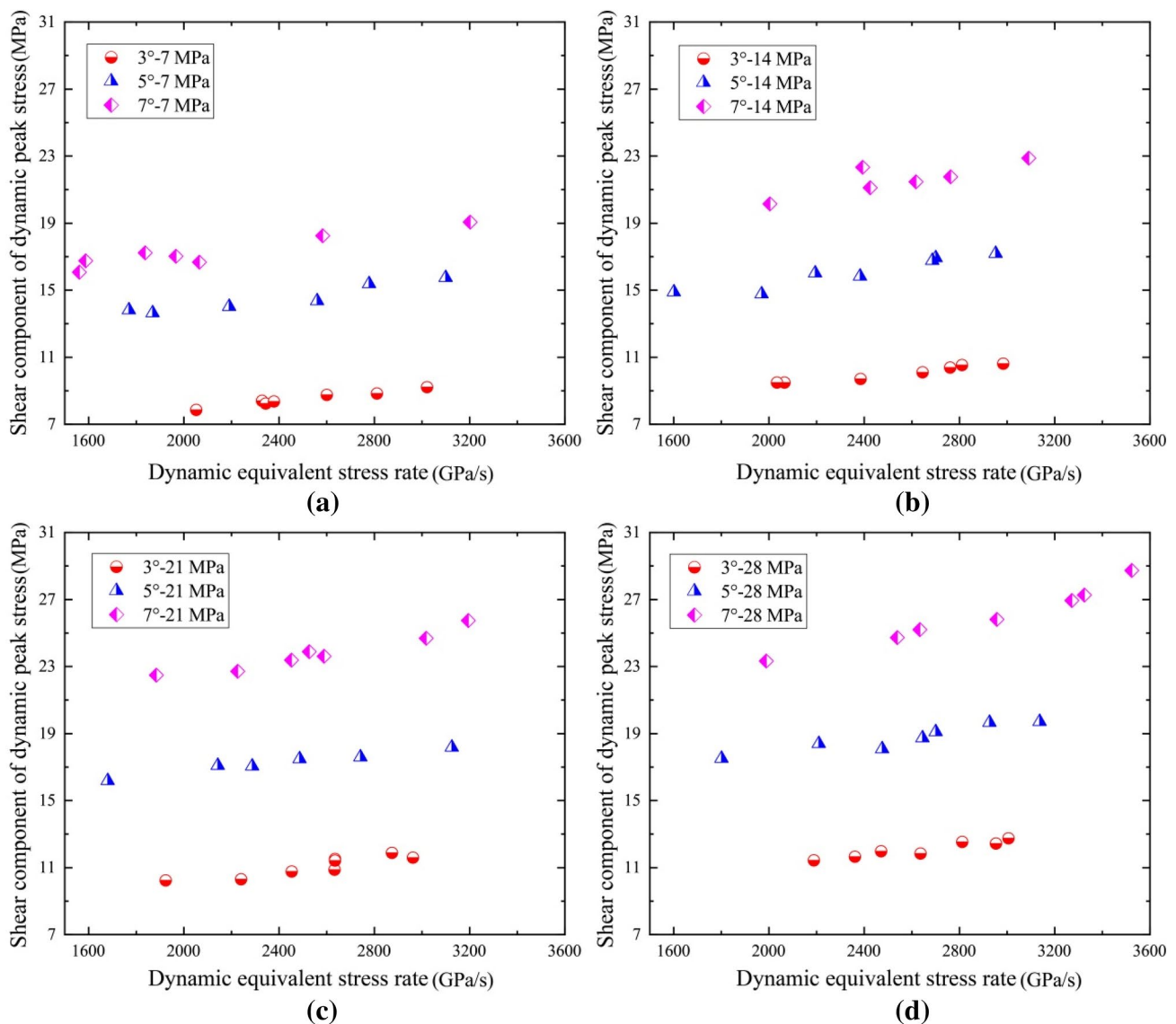


Fig. 10 Shear component of dynamic peak stress of the rock specimens with different inclination angles under various hydrostatic confining pressures

compression–shear impacting, the rock specimens fragmented at the dynamic equivalent stress rate of ~2600 GPa/s are manually sieved with the mesh sizes from 1 to 30 mm. Figure 14 depicts the cumulative mass fraction curves of the fragmented sandstone specimens with inclination angles of 3°, 5°, and 7° under hydrostatic confining pressures of 7, 14, 21 and 28 MPa. It can be observed that the fragments of the inclined specimens are larger for a higher inclination angle, suggesting that the shear component of dynamic loading restricts the fracture of hydrostatically confined rocks. Comparing the cumulative mass fraction curves of rock specimens with the same inclination angle, one can find that the rock specimens are fragmented more significantly at lower hydrostatic confining pressures. The rock fracture behavior

is generally restricted by the confining pressure and the shear component in the dynamic load.

The hydrostatically pressurized rock specimens under different compression–shear impacting have different failure patterns, as evidenced by the post-mortem examination of the recovered specimens. Figure 15 demonstrates the failure patterns of the rock specimens with inclination angles of 3°, 5°, and 7° under hydrostatic confining pressures of 7, 14, 21, and 28 MPa, respectively. At a low confining pressure, the angle between the fracture path on the specimen surface and the loading direction increases as the shear/compression ratio increases, indicating that the surface failure mode changes from the tensile-dominated failure to the shear-dominated failure. For the specimens with inclination angles of

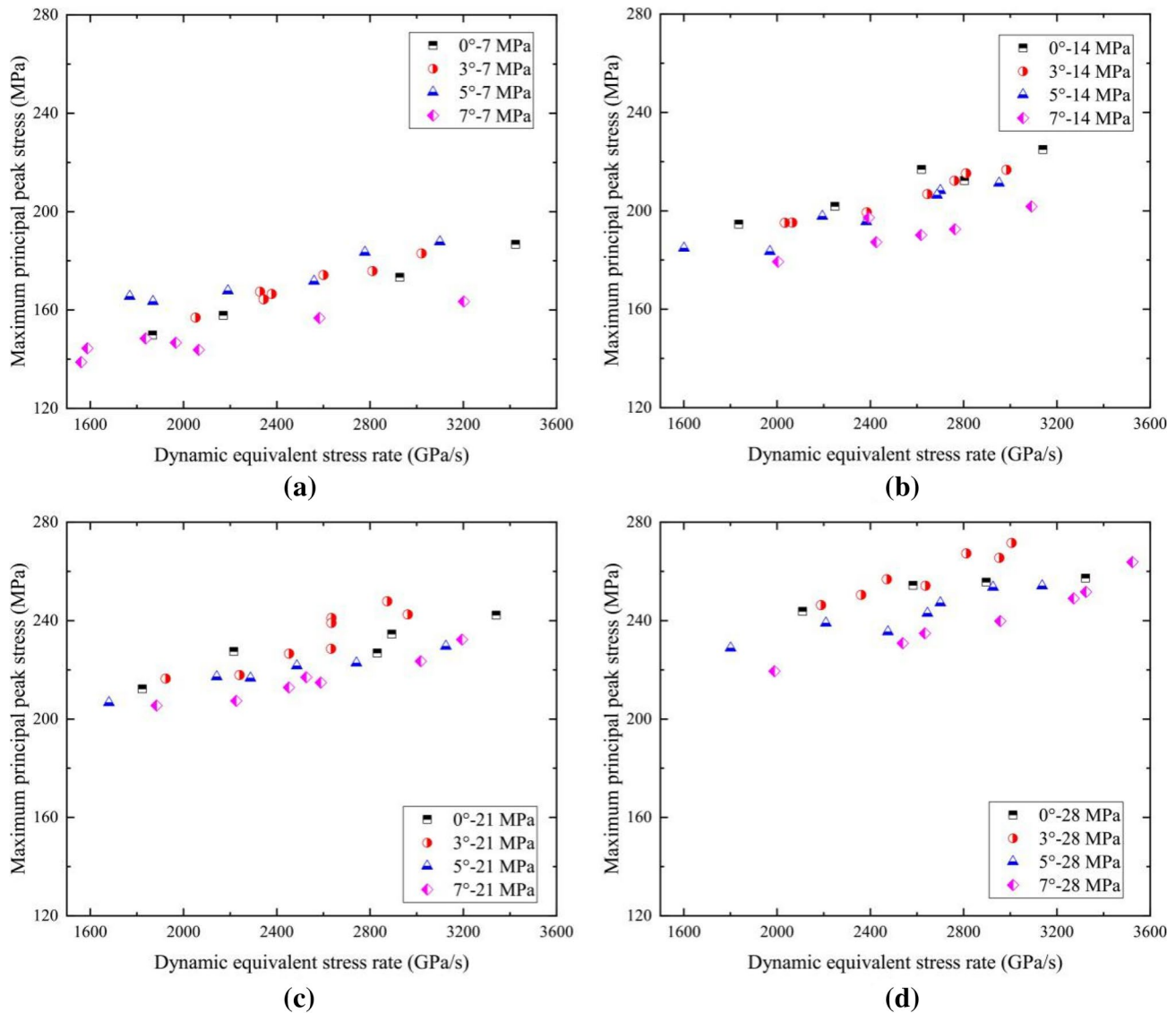


Fig. 11 Variation of the maximum principal peak stress of the rock specimens versus the dynamic equivalent stress rate under different hydrostatic confining pressures

3°, 5°, and 7°, the inner fracture surfaces are, respectively, a truncated conical surface, two cambered shear surfaces with a small inclination, and a single cambered shear surface. At a relatively high confining pressure, as the specimen inclination angle increases to 5°, the fracture surface of the specimen under combined compression–shear impacting changes from two slightly inclined cambered shear surfaces to a single shear surface along the short diagonal of the oblique specimen. The shear failure surface of the 7° oblique specimen is not as cambered as that of the 3° and 5° oblique specimens but looks more even and regular. It can thus be concluded that, as the shear/compression ratio and the hydrostatic confining pressure increase, the failure pattern of the rock specimen under compression–shear impacting

changes from the tensile-dominated failure with a truncated conical surface to the shear-dominated failure with a single shear plane along its short diagonal.

4 Conclusions

In this study, the dynamic tests are conducted on inclined cylindrical sandstone specimens with hydrostatic confining pressures to reveal the dynamic compression–shear responses and failure criterion of hydrostatically pressurized rocks. Our experimental results demonstrate the comprehensive effects of the shear/compression ratio, hydrostatic confining pressure and dynamic loading rate on the

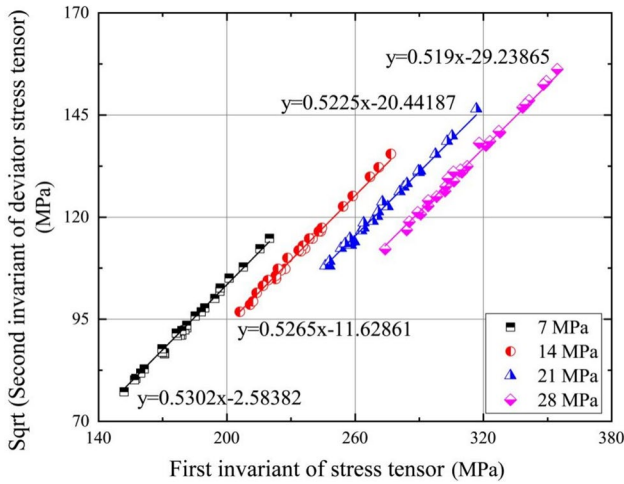


Fig. 12 Failure surfaces of the hydrostatically pressurized rock specimens under combined compression–shear loading on the basis of the D–P failure criteria in the $I_1 - \sqrt{J_2}$ plane

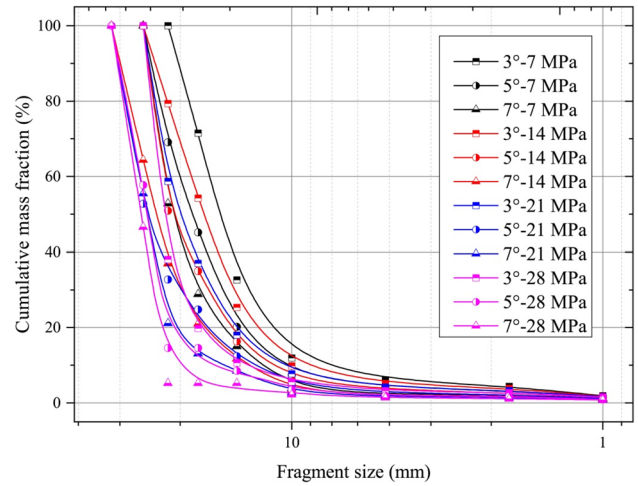


Fig. 14 Cumulative mass fraction curves of the fragmented rock specimens

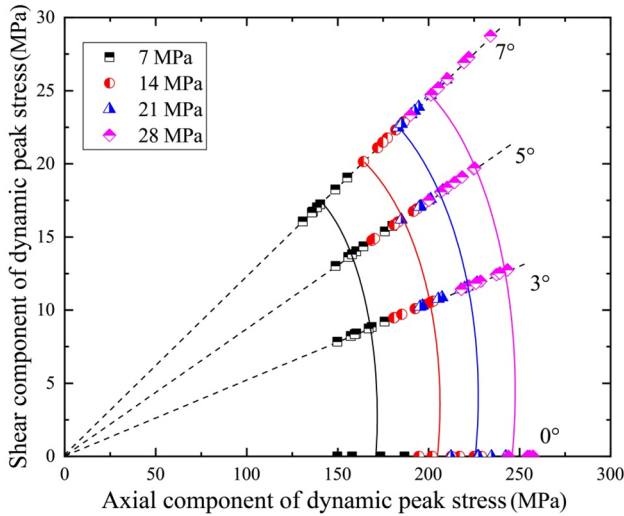


Fig. 13 Failure surfaces of the hydrostatically pressurized rock specimens under combined compression–shear loading on the basis of the D–P failure criteria in the $\sigma - \tau$ plane

dynamic mechanical responses of rocks, including the axial and shear components of dynamic peak stress, deformation

behavior, and fragmentation and failure patterns. The main conclusions are as follows:

1. The dynamic peak stress of rocks shows evident loading path effect and hydrostatic confining dependence, and the failure surface based on the D–P criterion under such loading conditions expands outwards gradually as the hydrostatic confining pressure increases.
2. The compressive deformation modulus of rocks decreases as the shear component of dynamic loading increases, utterly contrary to its response to the confining pressure. The confining pressure enhances the weakening effect of the shear component in dynamic load on the compressive deformation modulus.
3. Fragmentation analysis indicates that the hydrostatic confining pressure and the shear component of dynamic loading restrict the fracture behavior of rocks, and the hydrostatic confining pressure enhances the restriction of the shear component on rock fragmentation.
4. As the shear/compression ratio of dynamic load and the hydrostatic confining pressure increase, the failure pattern of the rock specimen changes from the tensile-dominated failure with a truncated conical surface to the shear-dominated failure with a single shear plane along its short diagonal.

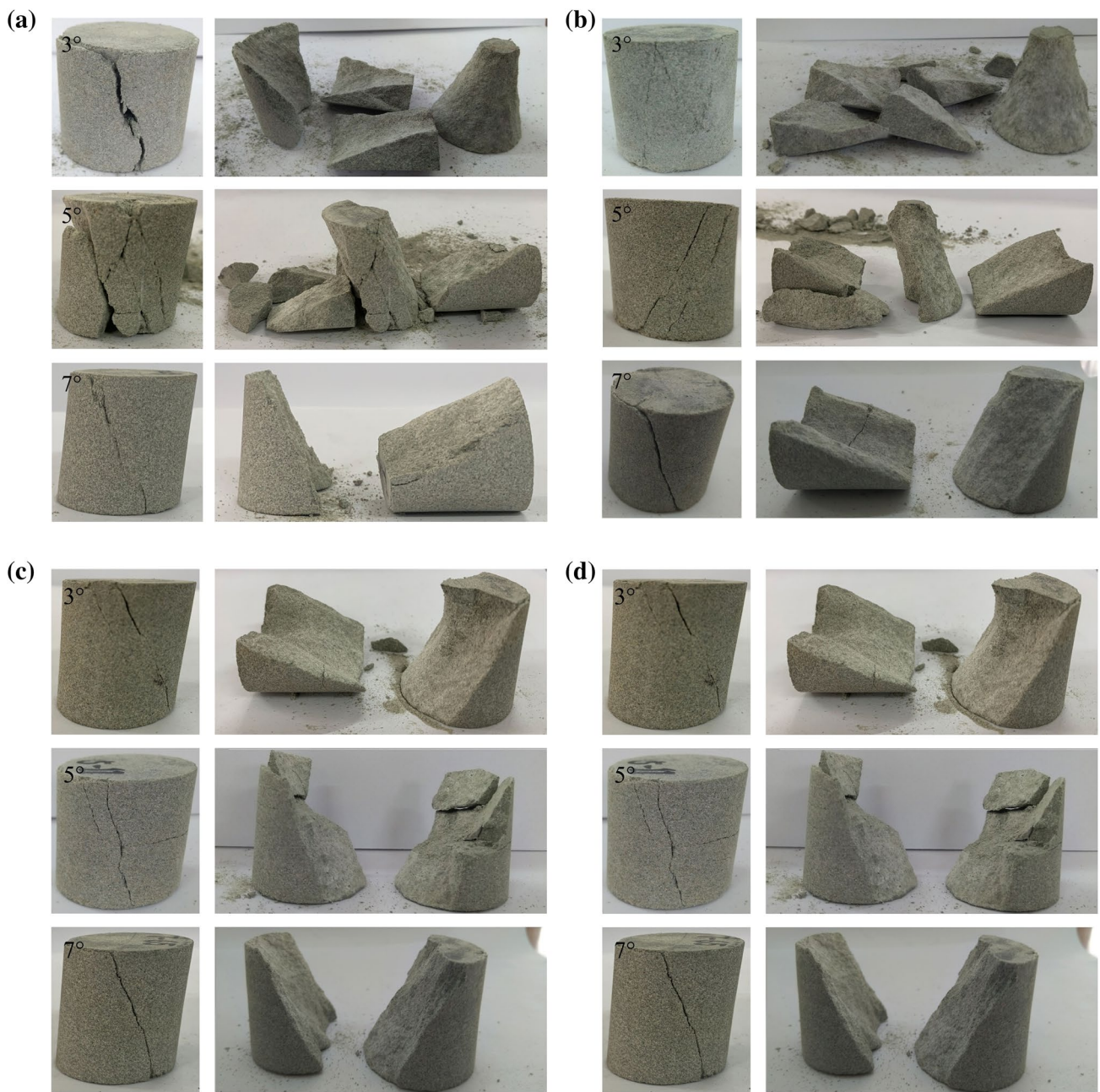


Fig. 15 Failure patterns of the specimens with inclination angles of 3°, 5°, and 7° under hydrostatic confining pressures of **a** 7 MPa, **b** 14 MPa, **c** 21 MPa, and **d** 28 MPa

Acknowledgements The authors thank the financial support from the National Natural Science Foundation of China (Nos. 52039007 and 51779164).

References

- Bailly P, Delvare F, Vial J, Hanus JL, Biessy M, Picart D (2011) Dynamic behavior of an aggregate material at simultaneous high pressure and strain rate: SHPB triaxial tests. *Int J Impact Eng* 38(2–3):73–84
- Chen R, Yao W, Lu F, Xia K (2018) Evaluation of the stress equilibrium condition in axially constrained triaxial SHPB tests. *Exp Mech* 58(3):527–531
- Dai F, Huang S, Xia K, Tan Z (2010) Some fundamental issues in dynamic compression and tension tests of rocks using split hopkinson pressure bar. *Rock Mech Rock Eng* 43(6):657–666
- Drucker DC, Prager W (1952) Soil mechanics and plastic analysis or limit design. *Q Appl Math* 10(2):157–165

- Du K, Tao M, Li X, Zhou J (2016) Experimental study of slabbing and rockburst induced by true-triaxial unloading and local dynamic disturbance. *Rock Mech Rock Eng* 49(9):3437–3453
- Du H, Dai F, Xu Y, Liu Y, Xu H (2018) Numerical investigation on the dynamic strength and failure behavior of rocks under hydrostatic confinement in SHPB testing. *Int J Rock Mech Min* 108:43–57
- Du H, Dai F, Xu Y, Yan Z, Wei M (2020a) Mechanical responses and failure mechanism of hydrostatically pressurized rocks under combined compression-shear impacting. *Int J Mech Sci* 165:105219
- Du H, Dai F, Liu Y, Xu Y, Wei M (2020b) Dynamic response and failure mechanism of hydrostatically pressurized rocks subjected to high loading rate impacting. *Soil Dyn Earthq Eng* 129:105927
- Duan K, Li Y, Wang L, Zhao G, Wu W (2019) Dynamic responses and failure modes of stratified sedimentary rocks. *Int J Rock Mech Min* 122:104060
- Foroughi MH, Vutukuri VS (1997) Estimating elastic pillar stresses in inclined coal seams. *Trans Soc Min Metall Explor Inc* 302:50–54
- Frew DJ, Forrestal MJ, Chen W (2001) A split Hopkinson pressure bar technique to determine compressive stress-strain data for rock materials. *Exp Mech* 41(1):40–46
- Frew DJ, Forrestal MJ, Chen W (2002) Pulse shaping techniques for testing brittle materials with a split Hopkinson pressure bar. *Exp Mech* 42(1):93–106
- Frew DJ, Akers SA, Chen W, Green ML (2010) Development of a dynamic triaxial kolsky bar. *Meas Sci Technol* 21. <https://doi.org/10.1088/0957-0233/21/10/105704>
- Gong F, Si X, Li X, Wang S (2019) Dynamic triaxial compression tests on sandstone at high strain rates and low confining pressures with split hopkinson pressure bar. *Int J Rock Mech Min* 113:211–219
- Greensmith BJT (1983) Petrology of the sedimentary rocks. *J Geol* 6: <https://doi.org/10.1007/978-94-011-9640-6>
- Hokka M, Black J, Tkalich D et al (2016) Effects of strain rate and confining pressure on the compressive behavior of kuru granite. *Int J Impact Eng* 91:183–193
- Hopkinson B (1914) A method of measuring the pressure produced in the detonation of high explosives or by the impact of bullets. *Philos Trans R Soc Lond Ser A Contain Pap Math Phys Char* 213:437–456
- Hou B, Ono A, Abdennadher S, Pattofatto S, Li YL, Zhao H (2011) Impact behavior of honeycombs under combined shear-compression. Part I: experiments. *Int J Solids Struct* 48(5):687–697
- Hou B, Xiao R, Sun TF et al (2019) A new testing method for the dynamic response of soft cellular materials under combined shear-compression. *Int J Mech Sci* 159:306–314
- Kolsky H (1949) An investigation of the mechanical properties of materials at very high rates of loading. *Proc Phys Soc Sect B* 62(11):676–700
- Li X, Zhou Z, Lok T, Hong L, Yin T (2008) Innovative testing technique of rock subjected to coupled static and dynamic loads. *Int J Rock Mech Min* 45(5):739–748
- Li X, Gong F, Tao M et al (2017) Failure mechanism and coupled static-dynamic loading theory in deep hard rock mining: a review. *J Rock Mech Geotech Eng* 9(4):767–782
- Li Y, Wu W, Tang C, Liu B (2019) Predicting the shear characteristics of rock joints with asperity degradation and debris back-filling under cyclic loading conditions. *Int J Rock Mech Min* 120:108–118
- Martin BE, Kabir ME, Chen W (2013) Undrained high-pressure and high strain-rate response of dry sand under triaxial loading. *Int J Impact Eng* 54:51–63
- Nie X, Chen WW, Sun X, Templeton DW (2007) Dynamic failure of borosilicate glass under compression/shear loading experiments. *J Am Ceram Soc* 90(8):2556–2562
- Perkins RD, Green SJ, Friedman M (1970) Uniaxial stress behavior of porphyritic tonalite at strain rates to 103/second. *Int J Rock Mech Min* 7(5):527
- Rahimi R, Nygaard R (2015) Comparison of rock failure criteria in predicting borehole shear failure. *Int J Rock Mech Min* 79:29–40
- Shen W, Zhao T, Crosta GB, Dai F (2017) Analysis of impact-induced rock fragmentation using a discrete element approach. *Int J Rock Mech Min* 98:33–38
- Sun X, Liu W, Chen W, Templeton D (2009) Modeling and characterization of dynamic failure of borosilicate glass under compression/shear loading. *Int J Impact Eng* 36(2):226–234
- Suorinen FT, Kaiser PK, Mgumbwa JJ, Thibodeau D (2011) Mining of orebodies under shear loading part 1 - case histories. *Min Technol* 120(3):137–147
- Suorinen FT, Mgumbwa JJ, Kaiser PK, Thibodeau D (2014) Mining of orebodies under shear loading part 2 - failure modes and mechanisms. *Min Technol* 123(4):240–249
- Wagner H (2019) Deep mining: a rock engineering challenge. *Rock Mech Rock Eng* 52(5):1417–1446
- Xia K, Nasser MHB, Mohanty B, Lu F, Chen R, Luo SN (2008) Effects of microstructures on dynamic compression of barre granite. *Int J Rock Mech Min* 45(6):879–887
- Xie H, Konietzky H, Zhou HW (2019) Special issue “deep mining.” *Rock Mech Rock Eng* 52(5):1415–1416
- Xu Y, Dai F (2018) Dynamic response and failure mechanism of brittle rocks under combined compression-shear loading experiments. *Rock Mech Rock Eng* 51(3):747–764
- Xu S, Huang J, Wang P, Zhang C, Zhou L, Hu S (2015) Investigation of rock material under combined compression and shear dynamic loading: an experimental technique. *Int J Impact Eng* 86:206–222
- Xu Y, Dai F, Du H (2020) Experimental and numerical studies on compression-shear behaviors of brittle rocks subjected to combined static-dynamic loading. *Int J Mech Sci* 175:105520
- Zhang QB, Zhao J (2014) A review of dynamic experimental techniques and mechanical behaviour of rock materials. *Rock Mech Rock Eng* 47(4):1411–1478
- Zhao PD, Lu FY, Chen R et al (2011) A technique for combined dynamic compression-shear test. *Rev Sci Instrum* 82(3):35110
- Zhao PD, Lu FY, Lin YL, Chen R, Li JL, Lu L (2012) Technique for combined dynamic compression-shear testing of PBXs. *Exp Mech* 52(2):205–213
- Zhao Z, Peng H, Wu W, Chen Y (2018) Characteristics of shear-induced asperity degradation of rock fractures and implications for solute retardation. *Int J Rock Mech Min* 105:53–61
- Zhou YX, Xia K, Li XB et al (2012) Suggested methods for determining the dynamic strength parameters and mode-I fracture toughness of rock materials. *Int J Rock Mech Min* 49:105–112

Publisher's Note Springer Nature remains neutral with regard to jurisdictional claims in published maps and institutional affiliations.